*universe*

MDPI

*Article*

# Research on Physics-Informed Transformer for Space Object Shape Classification

**Mengci Li [1,2], Laixian Zhang [1,2,*], Rong Li [1,2], Yingchun Li [1,2], Shiyu Deng [3,4], Huichao Guo [1,2], Haijing Zheng [1,2], Huaili Zhang [1,2], Yang Zhao [1,2], Zhen Deng [1,2] and Rui Zhu [1,2]**

1 National Key Laboratory of Space Target Awareness, Space Engineering University, Beijing 101416, China; mengcili@hgd.edu.cn (M.L.); bitlirong@163.com (R.L.); 100654_gd@hgd.edu.cn (Y.L.); guohuichaoo@163.com (H.G.); zhenghj@hgd.edu.cn (H.Z.); bjzhanghl@163.com (H.Z.); zyang2023@hgd.edu.cn (Y.Z.); 200317@hgd.edu.cn (Z.D.); 200347@hgd.edu.cn (R.Z.)
2 Key Laboratory of Intelligent Space TTC&O Ministry of Education, Space Engineering University, Beijing 101416, China
3 Changchun Observatory of National Astronomical Observators, Chinese Academy of Sciences, Changchun 130117, China; dengsy@cho.ac.cn
4 National Astronomical Observators, Chinese Academy of Sciences, Beijing 100101, China
* Correspondence: zhanglaixian@pku.edu.cn

## Abstract

Estimating the shape of space objects helps infer key characteristics such as object type, mass, and potential operational status, thereby providing critical decision-making support for space threat assessment. This paper proposes a Physics-Informed Transformer deep learning model for space object shape classification based on photometric time series data. The model achieves a classification accuracy of 89.22% on a hybrid dataset combining simulated and measured data, outperforming eight classical models with an average accuracy improvement of 3.61%. Ablation experiments demonstrate that the introduction of physical gating yields an average accuracy improvement of 1.43%. Using evaluation metrics including the confusion matrix, PR curve, ROC curve, and confidence distribution histogram, we demonstrate that the model possesses high accuracy, strong robustness, and good interpretability.

**Keywords:** space object; shape classification; photometry; deep learning

## 1. Introduction

With the rapid advancements in aerospace technology, the number of spacecraft in outer space has increased significantly, imposing higher demands on monitoring capabilities [1]. Space Situational Awareness (SSA) encompasses the activities and processes involved in the acquisition and processing of space object information, the generation and application of situational awareness products, and the monitoring of the space environment [2]. It serves as a critical link in obtaining space information. Estimating the shape of space objects has emerged as a vital component in contemporary SSA research. The configuration of these space objects is of particular interest, as it enables the inference of key characteristics such as object type, mass, and potential operational status, thereby providing a critical decision-making basis for space threat assessment [3,4]. Investigations indicate that the most common shape among space objects is a box shape. For typical satellites such as box-wing satellites and CubeSats, the satellite platform or main body can be abstracted as a three-dimensional cubic structure [1]. Certain satellites exhibit

Check for updates

Academic Editor: Lorenzo Iorio

Received: 11 May 2026
Revised: 7 July 2026
Accepted: 13 July 2026
Published: 15 July 2026

**Copyright:** © 2026 by the authors. Licensee MDPI, Basel, Switzerland. This article is an open access article distributed under the terms and conditions of the Creative Commons Attribution (CC BY) license.

other shapes. For example, some Starlink and other low-Earth-orbit mega-constellation satellites are flat-panel-shaped [5], some laser ranging satellites are spherical [6], and some spin-stabilized satellites and rocket bodies are cylindrical [7].

Ground-based optical systems have become a popular means of obtaining space object information, particularly for medium and high Earth orbit objects, within the space situational awareness (SSA) community [8,9]. These systems provide photometric measurements of space objects, and when combined with established light curve inversion techniques, where the observed brightness over time serves as the basis for recovering underlying physical characteristics, they enable obtaining characterizations such as object shape [10].

Currently, the main research in the field includes three-dimensional (3D) surface reconstruction and shape classification of space objects. 3D surface reconstruction primarily involves inverting the three-dimensional shape of a space object from its light curve, generating a concave–convex surface, with the final output being a three-dimensional mesh model of the object [11]. These mainly include nonlinear filtering-based inversion methods [12] such as the Unscented Kalman filter (UKF) [12–14], Unscented Schmidt Kalman filter (USKF) [14,15], particle filter (PF) [16], multiple model adaptive estimation (MMAE) [11,17,18], and hierarchical mixtures of experts (HME) [19,20]; the Gaussian surface density-based shape inversion method [3,21,22]; and the two-facet model-based inversion method [23,24]. These methods often rely on prior information such as target aspect angle [14], orbit [25], rotation state [21], and shape template [25]. Moreover, most algorithms are better suited for convex objects and perform poorly on non-convex objects [22]. In recent years, Robinson has proposed an inversion method incorporating angular velocity that is applicable to non-convex objects [26], and Tang has proposed a deep learning-based inversion method for asteroid shapes; however, these methods still depend on prior information [27].

For non-cooperative targets, prior models are difficult to obtain, and one can only rely on passive observational data to infer target attributes. Shape classification methods for space objects can address the issue of dependence on prior information. Traditional light curve classification methods fall into two categories. One approach is manual classification based on the overall characteristics of the light curve [28–30]. The other approach uses light curves or extracted features in combination with machine learning or deep learning algorithms [31]—such as Naïve Bayes [32], logistic regression [32], random forests (RF) [32,33], support vector machines (SVM) [32–35], neural network [32], CN2 rule induction [32], k-nearest neighbors (KNN) [32,33], hierarchical clustering [34], recurrent neural networks (RNN) [36], convolutional neural networks (CNN) [33,35,37], deep neural networks (DNN) [38], bagged decision trees (Bagged Trees) [35], and fully convolutional neural network (FCN) [39]—to train on the curves or extracted parameters, thereby obtaining the class of object. In recent years, Allworth has classified different shapes of space debris using CNN-based classification and transfer learning methods [40]. Lu employed a hierarchical classification method combining CNN and RF to perform fine-grained classification of object models, thereby achieving basic shape classification of space debris [7]. Kerr used CNN to classify object shapes such as spheres, box objects, and box-wing configurations [41]. Badura proposed a method for identifying the maneuver status of space objects that combines physical models with CNN [42]. Qashoa conducted related research based on Long Short-Term Memory networks (LSTMs) [43]. Zhang proposed a CNN classification algorithm using space-based optical simulation images to classify satellites and debris [44]. Wang proposed a ResNet-based classification algorithm for cubes (in-orbit satellites), cones (rocket bodies), and ellipsoids (space debris) [1]. Majhi proposed a debris and satellite classification algorithm that incorporates orbital parameters [45]. Adri-

ano proposed a shape classification algorithm for space debris using a Long Short-Term Memory Fully Convolutional Network (LSTM-FCN) [10].

Most of the above algorithms are based on improved deep learning methods such as CNN [1,4,7,40–42,44], which possess strong feature extraction capabilities and high accuracy, achieving performance superior to traditional approaches. Some algorithms incorporate orbital elements [45], optical images [44], and other information to enhance classification accuracy. A few algorithms integrate physical models but do not specifically address object shape classification [42]. Considering the 'black-box' nature of deep learning, which leads to models lacking physical information, this paper proposes a Physics-Informed Transformer (PIT) model. This model does not require information such as orbital parameters. After feature encoding, the encoded features serve as gating signals that dynamically modulate the output of the multi-head attention mechanism in the Transformer. This enables the model to capture long-range dependencies in sequences, improve model accuracy, reduce generalization error, and embed physical priors into the deep learning framework.

The structure of this paper is organized as follows: In Section 2, we introduce a PIT model capable of classifying space object shapes based on light curves. In Section 3, we describe the simulation data, measured data, and experimental procedures. In Section 4, we analyze the experimental results. In Section 5, we present the conclusions.

## 2. Physics-Informed Transformer Model

We propose a Physics-Informed Transformer model that deeply integrates the physical features of object photometric sequences with the self-attention mechanism, constructing an end-to-end shape recognition model that possesses both data fitting capability and physical consistency. It addresses the issues of weak generalization and poor interpretability commonly found in traditional data-driven models, which tend to neglect physical priors. The multi-head physics-aware self-attention mechanism incorporated in the model endows it with superior capability of capturing long-range dependencies compared to traditional LSTM and CNN algorithms.

### *2.1. Overall Model Architecture*

The PIT model aims to achieve robust classification of space object shapes by leveraging both temporal photometric features and physical knowledge of space objects. The model adopts a dual-branch encoding architecture: one branch employs a Transformer architecture to capture long-range dependencies in light curve sequences, while the other branch encodes either physical prior information or physical features extracted from the light curve as physical gating signals. Through a physics-aware attention mechanism, the physical features are embedded into the self-attention computation to dynamically modulate the output of the Transformer's multi-head attention. Finally, the shape category of the space object is output via a classification head, enabling joint modeling of data-driven and physics-based knowledge while maintaining the efficiency of end-to-end training. The model architecture is illustrated in Figure 1, which includes an input embedding layer, sequence encoding, physical encoding, Physics-Informed Transformer blocks, and a classification head.

The input embedding layer maps the preprocessed light curve $x \in R^{B\times N\times 1}$ (where $B$ is the batch size and $N$ is the sequence length) into a high-dimensional feature space via a linear projection, yielding $X_{proj} \in R^{B\times N\times C}$ (where $C$ is the feature dimension), thereby providing a foundation for subsequent positional encoding and Transformer encoding.

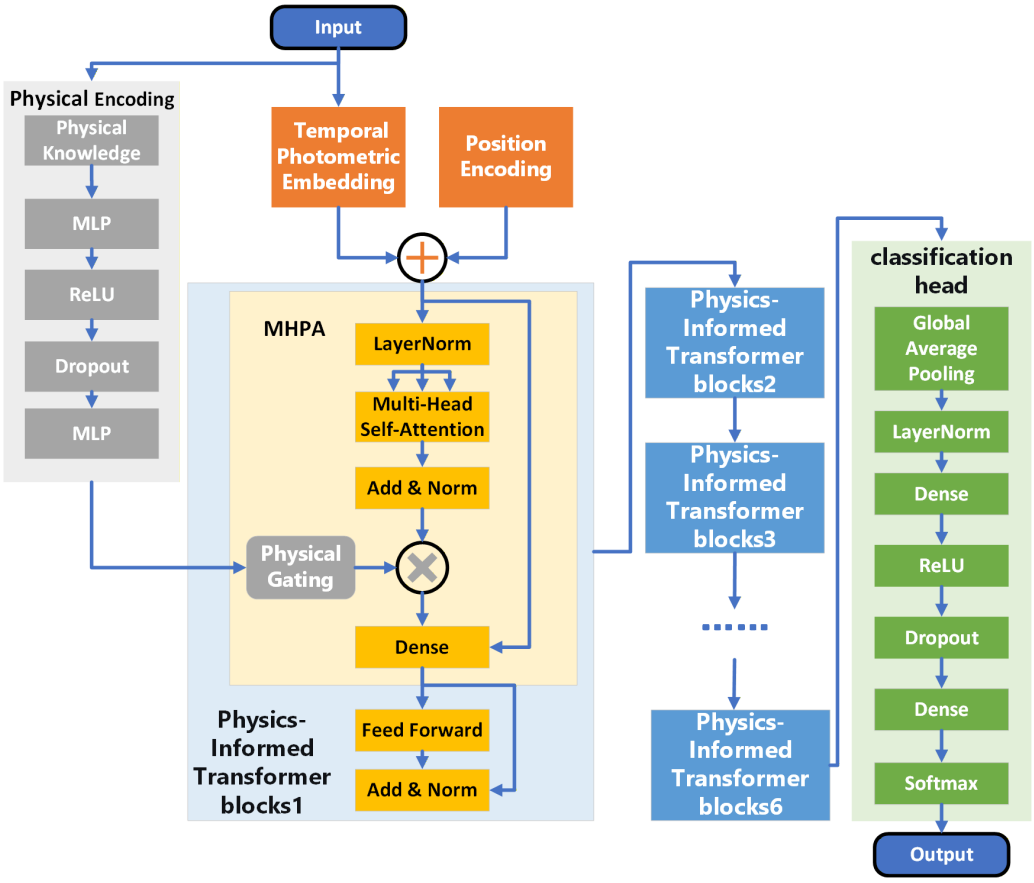



**Figure 1.** PIT model architecture. We input the preprocessed light curve into the model and then the PIT model outputs the shape classifications of space objects.

Sequence encoding combines the output of the input embedding layer with learnable positional information, enabling the model to perceive the sequential relationship of brightness values along the time axis, resulting in $X = X_{proj} + PosEmb \in R^{B\times N\times C}$.

The physical encoding process maps the physical features $f_{phy}$ to a physical embedding of the same dimension as the sequence via a two-layer Multilayer Perceptron (MLP), yielding $f_{embed} = PhysicalEncoder\left(f_{phy}\right)$. This embedding captures the global physical attributes of the object shape and serves as a gating signal injected into each physics-aware Transformer block, thereby enabling the continuous guidance of physical priors throughout the network.

The physics-aware Transformer block, which serves as the core encoding unit of the model, is stacked in 6 layers and consists of an improved multi-head physics-aware self-attention mechanism (MHPA) and a feed-forward network (FFN), as introduced in Sections 2.2 and 2.3.

The classification head applies global average pooling to the output $X_T$ of the last physics-aware Transformer block to obtain the global feature $X_{global}$, which is then fed into a classification layer to output the probabilities $\hat{y}$ for the four shape categories (box, flat-panel, sphere, cylinder), thereby accomplishing the classification task, as shown in Equations (1) and (2).

$$X_{global} = \frac{1}{N}\sum_{i=1}^{N} X_{T,i} \tag{1}$$

$$\hat{y} = Softmax\left(Classifier(X_{global})\right) = P(y \in \{\text{box, flat-panel, sphere, cylinder}\}|x, f_{phy}) \tag{2}$$

where $i$ is the temporal index of the sequence.

The model loss adopts standard cross-entropy. Physical constraints are implemented in an end-to-end embedding manner rather than as explicit loss terms, and a physics-gating mechanism is used to ensure that the output respects the physical priors of the object, as shown in Equation (3).

$$Loss = -\frac{1}{B}\sum_{i=1}^{B} y_i log\hat{y} \tag{3}$$

The physical embedding enables the model to maintain consistency in shape recognition even under low-data and high-noise scenarios.

### *2.2. Multi-Head Physics-Aware Self-Attention Mechanism*

Traditional self-attention relies solely on data correlation modeling, which can easily deviate from physical laws. This paper proposes an MHPA that weights the attention output with physical features in a gating manner, forcing the model to learn temporal dependencies under physical constraints.

The vector $X_{\mathrm{MNPA}} \in R^{B\times N\times C}$ input to MHPA is projected to obtain the query $Q$, key $K$, and value $V$ vectors, as shown in Equations (4)–(6).

$$Q = X_{MNPA}W_Q \tag{4}$$

$$K = X_{MNPA}W_K \tag{5}$$

$$V = X_{MNPA}W_V \tag{6}$$

where $W_Q$, $W_K$, and $W_V$ are the weight matrices of the attention mechanism, which are randomly initialized and continuously optimized during model training.

The sequential self-attention is shown in Equation (7).

$$\mathrm{Attention}(Q, K, V) = \mathrm{softmax}(\frac{QK^T}{\sqrt{d_k}})V \tag{7}$$

where $d_k$ is the head dimension, used for numerical stability.

The physics-aware self-attention (PA) adds a physical gate after the attention output, as shown in Equation (8). The nf-dimensional physical feature vector $p \in R^{B\times nf}$ is projected by a two-layer MLP to a 256-dimensional embedding $e \in R^{B\times 256}$. An unsqueeze operation adds a temporal dimension, yielding $R^{B\times 1\times 256}$, which is broadcast along the time axis to $R^{B\times N\times 256}$. This tensor is passed through a linear-Sigmoid gating network to produce a gating tensor of identical shape, which modulates the self-attention output element-wise, enabling dynamic, time-step-specific control informed by physical features.

$$PA = \mathrm{Attention}(Q, K, V) \odot \sigma\left(W_p f_{embed} + b_p\right) \tag{8}$$

where $\odot$ is element-wise multiplication, σ is the Sigmoid function, and $W_p, b_p$ are learnable parameters. The physical embedding is transformed via a linear layer and a Sigmoid function to produce gating weights of the same dimension as the sequence, which modulate the representation at each time step, enabling the model to enhance or suppress information at specific time steps based on physical features.

Finally, the features are split into $h$ heads, the physics-aware self-attention is computed in parallel for each head, and the outputs are concatenated to obtain the MHPA, as shown in Equation (9).

$$MHPA(X_{MNPA}, f_{embed}) = \sum_{i=1}^{h} Attention_i(Q_i, K_i, V_i)W_o \odot \sigma\left(W_p f_{embed} + b_p\right) \tag{9}$$

where $W_o$ is the output projection matrix.

MHPA not only captures the global temporal dependencies of light curves at the data level but also constrains, filters, and regularizes the attention features at the physical level, forming a unified attention mechanism that combines data-driven learning with physical constraints. This enables the model to maintain strong fitting capability while achieving physical consistency.

### *2.3. Physics-Informed Transformer Blocks*

The Physics-Informed Transformer blocks are the core encoding units of the PIT model, whose primary function is to fuse the temporal sequence features with the global physical attributes of the object, thereby achieving high-dimensional sequence representation learning guided by physical priors. Each Physics-Informed Transformer block consists of layer normalization, physics-aware attention, layer normalization, and a feed-forward network, and includes residual connections.

The sequence encoding vector $X$ and the physical encoding vector $f_{\text{embed}}$ are input into the first Physics-Informed Transformer block, and the resulting output $X_{T1}$ is shown in Equation (10).

$$X_{T1} = X + MHPA(LayerNorm(X), f_{embed}) + FFN(LayerNorm(X + MHPA(LayerNorm(X), f_{embed}))) \quad (10)$$

The feed-forward network consists of two fully connected layers with a hidden layer dimension of 1024 and uses the GELU activation function. The entire model stacks six such blocks, with eight heads and a dropout rate of 0.1.

Specifically, this module introduces a physics-aware attention mechanism, which applies gating weights generated from the physical embedding to the self-attention output within each Physics-Informed Transformer block, thereby dynamically adjusting the contribution strength of different feature channels to the currently encoded time step. This design enables the model, while capturing long-range dependencies in the light curve, to selectively enhance feature responses related to the physical attributes of the object shape and suppress task-irrelevant noise or interference. Furthermore, by stacking six layers of identical structure with residual connections and layer normalization, the Physics-Informed Transformer block progressively abstracts more discriminative sequence-level semantic representations, providing high-quality feature inputs for the subsequent classification head.

In summary, this module serves as a bridge between physical knowledge and data-driven feature learning, enhancing the model's classification performance and interpretability for space object shapes.

## 3. Experiment

### *3.1. Sample Data*

The sample data used in the experiments include both photometric simulation data and measured data of space objects. The sample classes in the dataset are box, flat-panel, sphere, and cylinder. Figure 2 shows examples of their photometric time series data. The x-axis is split into left and right segments to demonstrate two distinct observation intervals for the same target. The gap between them indicates unobserved time periods; for example, the object is beyond the visible arc or in the Earth's shadow.

The simulation data are generated using the Space Object Optical Characteristics Simulation System developed by Space Engineering University. One of the system's functions is to establish an orbital coordinate system based on the object's TLE data, transform to the body coordinate system according to attitude settings, compute the positional parameters of the Sun and the sensor in the body coordinate system, calculate the effective cross-sectional area using a spherical model, and obtain the apparent magnitudes of objects in combination with albedo calculations [46]. The simulation data can be generated under

precisely controlled conditions, covering multiple shapes, different attitudes, and motion characteristics, thereby providing sufficient and accurately labeled training samples to ensure that the model possesses the fundamental ability to recognize diverse shape classes. As shown in Figure 3, the simulated sample set includes 501 light curves of box objects, 494 light curves of flat-panel objects, 501 light curves of spherical objects, and 503 light curves of cylindrical objects.

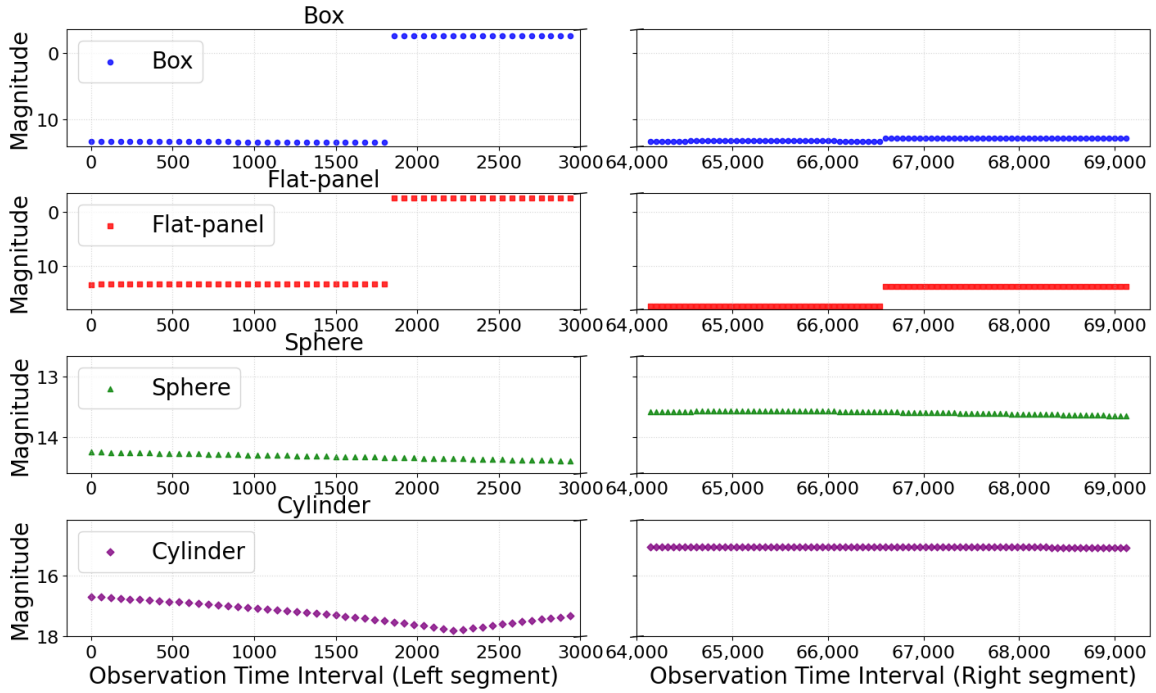



**Figure 2.** Examples of light curves of space objects with four distinct shapes.

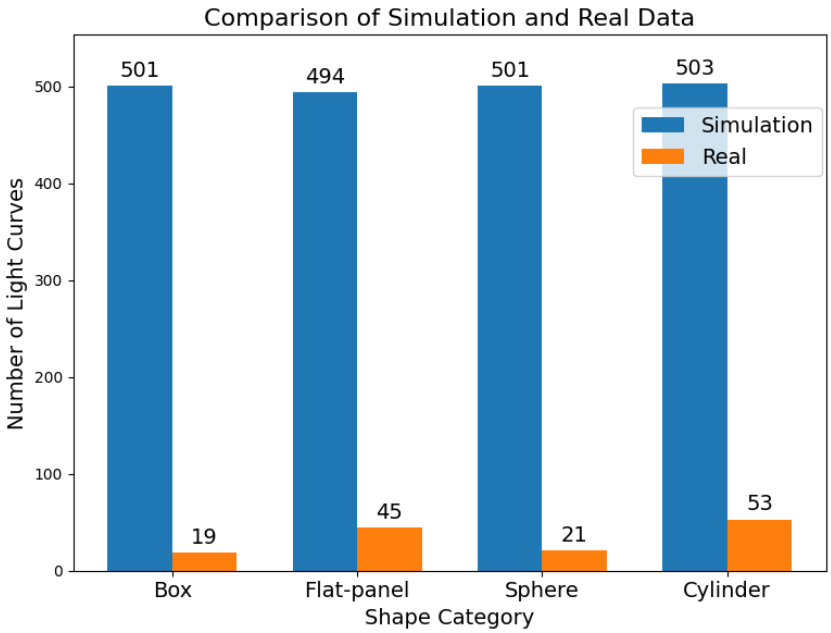



**Figure 3.** The volume of simulation and measured data.

The measured data mainly include time-domain photometric data obtained by the 260 mm optical telescope at Space Engineering University, as well as time-domain photometric data provided by the telescope at the Changchun Institute of Optics, Fine Mechanics and Physics, Chinese Academy of Sciences, and by the Changchun Observatory, National

Astronomical Observatories, Chinese Academy of Sciences. A small number of light curves from the Mini-MegaTORTORA (MMT) dataset are also included. These measured data from different observation stations reflect complex factors in real observational environments, such as atmospheric turbulence, stray light, detector noise, and station-specific environmental conditions, as well as the uncertainties in light curves caused by actual target attitude and orbital variations. To balance the class distribution of the measured data, historical light curves of 10 box objects, 11 flat-panel objects, 9 sphere objects, and 11 cylinder objects were adopted for the study. To capture multi-period rotational features and diverse observational geometries, light curves of the same object from adjacent passes within 48 h were concatenated. As shown in Figure 3, the measured sample set includes 19 light curves of box objects, 45 light curves of flat-panel objects, 21 light curves of spherical objects, and 53 light curves of cylindrical objects.

The combination of simulated and measured data provides both the sample richness required for supervised training and the generalization ability to real-world scenarios. The simulated data compensate for issues such as uneven sample distribution and scarcity of shape samples in the measured data, thereby improving model robustness. The measured data, on the other hand, are used to validate the model's effectiveness under real observational conditions and to avoid overfitting to simulated characteristics. This hybrid data strategy enables the model to fully learn physical features in a controlled environment while adapting to real observation conditions, thus achieving stronger generalization.

### *3.2. Physical Features*

Inspired by the physical characteristics of object shapes, we conduct experiments based on three types of physical features, namely Sequence Features, Frequency Domain Features, and Wavelet Features, totaling 19 features, as shown in Table 1. The formula is intended for feature extraction from light curves only when no prior information is available.

**Table 1.** Three types of physical features.

| Types | Features | Formulas |
|---|---|---|
| Sequence Features | Mean | $\mu = \frac{1}{N}\sum_{i=1}^{N} x_i$ |
| | Standard Deviation | $\sigma = \sqrt{\frac{1}{N}\sum_{i=1}^{N}(x_i-\mu)^2}$ |
| | Skewness | $skewness = \frac{1}{N}\sum_{i=1}^{N}\left(\frac{x_i-\mu}{\sigma}\right)^3$ |
| | Kurtosis | $kurtosis = \frac{1}{N}\sum_{i=1}^{N}\left(\frac{x_i-\mu}{\sigma}\right)^4 - 3$ |
| | Peak Ratio | $peakratio = \frac{P}{N}$<br>P is the total number of local peak points satisfying $x_i > x_{i-1}$ and $x_i > x_{i+1}$ |
| | Periodicity | $R(k) = \sum_{i=1}^{N-k}(x_i-\mu)(x_{i+k}-\mu)$<br>$periodicity = \frac{R(1)}{R(0)}$ |
| | Symmetry | $symmetry = corr(firsthalf, reverse(secondhalf))$<br>$firsthalf = x_{1:\lfloor\frac{N}{2}\rfloor}$, $secondhalf = x_{N-\lfloor\frac{N}{2}\rfloor+1:N}$ |
| | Entropy | $entropy = -\sum_{b} p_b \ln(p_b)$<br>$p_b$ is the statistical probability of each interval when the signal values are equally divided into 10 bins, with $p_b > 0$. |
| | Roughness | $roughness = std(x_2-x_1, x_3-x_2, \cdots, x_N-x_{N-1})$ |
| | Regularity | $A_k = \lvert FFT(x)\rvert_k, k = 1, \cdots, \left\lfloor\frac{N}{2}\right\rfloor$<br>$regularity = \frac{\sigma_A}{\mu_A}$ |

**Table 1.** *Cont.*

| Types | Features | Formulas |
|---|---|---|
| Frequency Domain Features | Spectrum Mean | $fft_{mean} = \frac{1}{M}\sum_{k=1}^{M} A_k$ <br> $M = \left\lfloor \frac{N}{2} \right\rfloor$ |
| | Spectrum Standard Deviation | $fft_{std} = \sqrt{\frac{1}{M}\sum_{k=1}^{M}(A_k - \mu_A)^2}$ |
| | Spectrum Peak Value | $fft_{peak} = \max_k A_k$ |
| | Spectrum Peak Frequency | $fft_{peakfreq} = \frac{\operatorname{argmax}_k A_k}{M}$ |
| | Spectral Entropy | $p_k = \frac{A_k}{\sum_{j=1}^{M} A_j}$ <br> $fft_{entropy} = -\sum_{k=1}^{M} p_k \ln(p_k + \epsilon)$ <br> $\epsilon$ is an infinitesimally small value. |
| Wavelet Features | cA3 Energy | $E_{cA3} = \frac{1}{L_{cA3}}\sum_{i=1}^{L_{cA3}}(cA3[i])^2$ |
| | cD3 Energy | $E_{cD3} = \frac{1}{L_{cD3}}\sum_{i=1}^{L_{cD3}}(cD3[i])^2$ |
| | cD2 Energy | $E_{cD2} = \frac{1}{L_{cD2}}\sum_{i=1}^{L_{cD2}}(cD2[i])^2$ |
| | cD1 Energy | $E_{cD1} = \frac{1}{L_{cD1}}\sum_{i=1}^{L_{cD1}}(cD1[i])^2$ |

There are 10 sequence features, which reflect the amplitude distribution, morphology, and fluctuation patterns of the signal. There are 5 frequency-domain features, which describe the energy distribution and structure of the signal in the frequency domain. There are 4 wavelet features, which capture the overall trend energy at the lowest frequency and largest scale, as well as the detail energy from high to medium frequencies, thereby characterizing the abrupt changes and oscillations of light curves across different time scales.

These 19 features constitute a multi-scale physical feature descriptor, capable of capturing amplitude distribution and global morphology, as well as revealing periodicity, spectral structure, and multi-resolution variations in the signal. For objects with historical data or other prior information, their physical features can be directly adopted; for objects without prior information, the features can be derived from light curves.

### *3.3. Experimental Procedure*

The complete experimental procedure is shown in Figure 4.

Step 1: Preprocess the light curve. First, perform sequence resampling to eliminate inconsistencies in the original file lengths. Then, apply a Savitzky–Golay filter to the resampled sequence to smooth the curve and suppress high-frequency observation noise, while preserving the overall trend and peak morphology as much as possible. Finally, perform global normalization to eliminate differences in absolute brightness values.

Step 2: For objects with prior information, concatenate their physical features; for objects without prior information, extract and concatenate physical features.

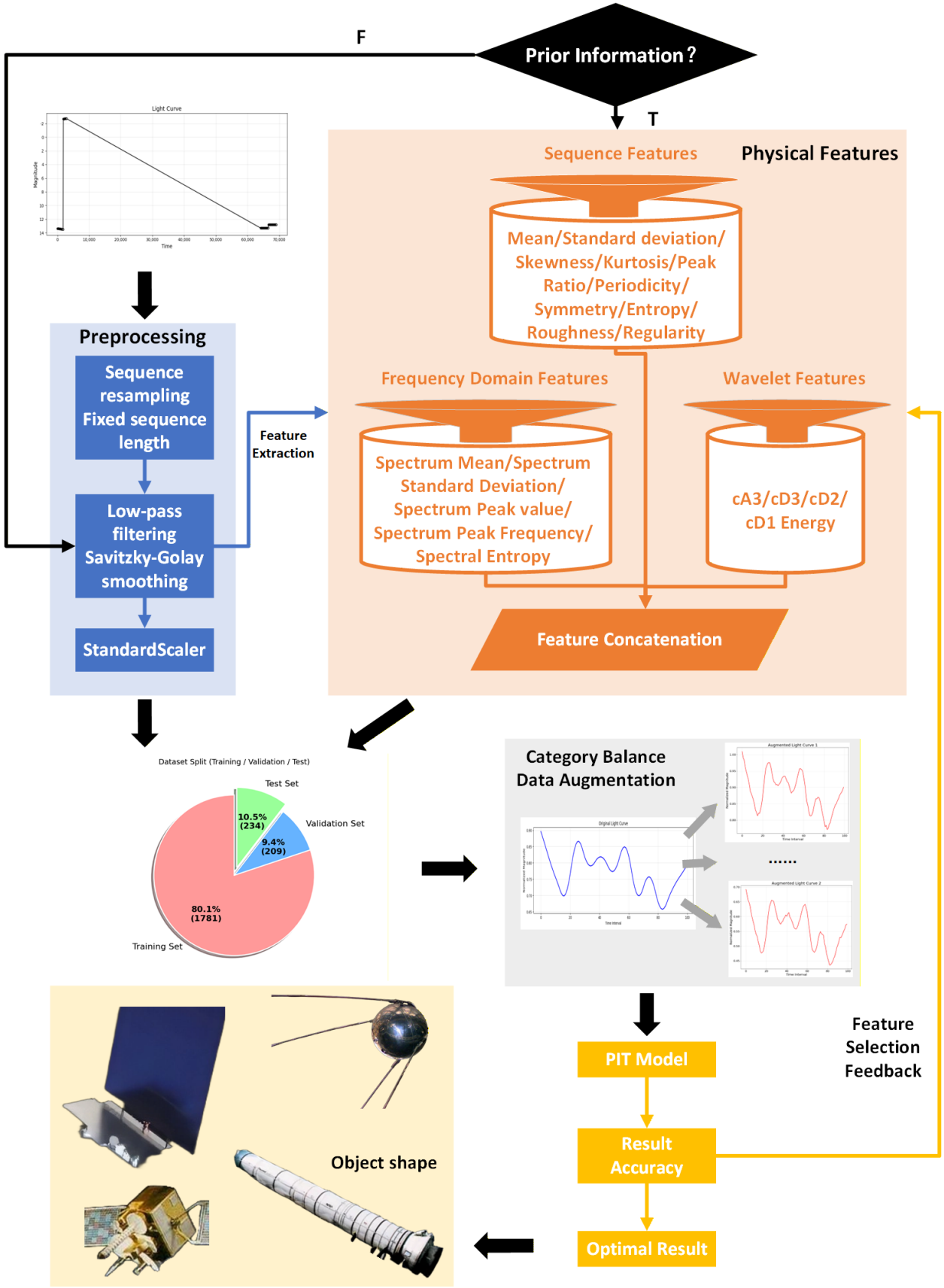



**Figure 4.** Experimental procedure.

Step 3: The dataset was partitioned in an 8:1:1 ratio into training, validation, and test sets. For the simulated data, the dataset was partitioned strictly in accordance with the

designated ratio. To prevent leakage of near-duplicate samples, it is necessary to avoid segments of the same pass from being distributed across different datasets. Light curves of the same measured object acquired on different days were grouped together into the same dataset. Priority was given to ensuring that each split contained all four object classes, rather than strictly adhering to the proportional requirements. Consequently, the training set comprised 1782 light curves, including light curves of 90 measured objects, specifically 12 light curves of box objects, 26 light curves of flat-panel objects, 10 light curves of sphere objects, and 42 light curves of cylinder objects. The validation set consisted of 210 light curves, including light curves of 21 measured objects, specifically 5 light curves of box objects, 8 light curves of flat-panel objects, 3 light curves of sphere objects, and 5 light curves of cylinder objects. The test set contained 232 light curves, including light curves of 23 measured objects, specifically 2 light curves of box objects, 11 light curves of flat-panel objects, 4 light curves of sphere objects, and 6 light curves of cylinder objects.

Step 4: Apply data augmentation methods to expand the dataset and address class imbalance. The augmentation method consists of adding Gaussian noise to the original data combined with amplitude scaling. The standard deviation of the Gaussian noise is set to 5% of the standard deviation of the original curve, and the scaling factor ranges from 0.9 to 1.1. The number of synthetic samples for each class is inversely proportional to the number of original samples to mitigate the class imbalance problem. To prevent any potential data leakage, the synthetic data augmentation was applied only to the training set, leaving the validation and test sets strictly unaugmented. After data augmentation, the training set comprised 2224 light curves, with 556 curves for each of the four object classes, thereby achieving class balance.

Step 5: The PIT model is trained on the input data. Based on the accuracy of the output results, feedback is provided to the physical feature module for feature selection.

Step 6: Obtain the object shape category based on the optimal model results.

## 4. Result Analysis

All algorithms were trained on Windows using the PyTorch 2.4.1 framework. The model employed the cross-entropy loss function with the AdamW optimizer using a learning rate of 0.001 and weight decay set to default. The learning rate was scheduled using cosine annealing. The training was conducted for 500 epochs with a batch size of 32. During training, the model parameters with the highest validation accuracy were saved. The extracted physical features were adjusted based on the model results to establish the optimal model, and the corresponding results are shown in Figure 5. All models achieved relatively high accuracy, demonstrating the effectiveness of the proposed algorithm. Among them, the model based solely on sequence features achieved the highest accuracy. This may be because wavelet features are extremely sensitive to parameter selection, and some of the prior data parameters were not sufficiently matched to the object, thereby affecting the result accuracy. Meanwhile, frequency domain features are susceptible to noise, which introduces errors and leads to degraded model performance.

The training results of the optimal model are shown in Figure 6, where the horizontal axis represents the training epoch. The left subplot shows the training loss, and the right subplot shows the validation accuracy. The training loss rapidly decreased from 1.0564 at epoch 1 to 0.0119 at epoch 500, while the validation accuracy gradually increased from 67.62% to 87.14% and remained stable in the later stage, demonstrating model convergence. The best validation accuracy of 88.57% was achieved at epoch 333. The minimum loss was similar across repeated training runs.

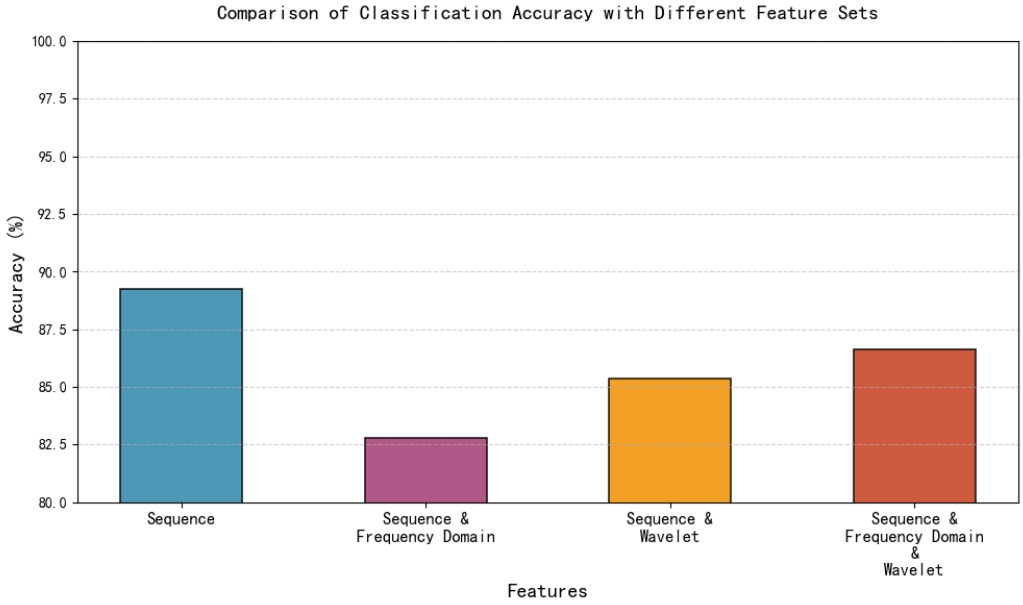



**Figure 5.** Model accuracy for different physical features.

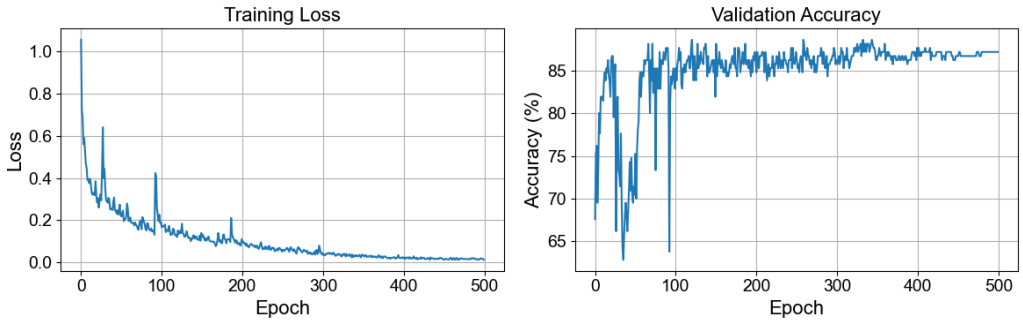



**Figure 6.** Training loss and validation accuracy curves of the optimal PIT model.

The examples of the classification results of the optimal PIT model for ten random space objects are shown in Figure 7. In each subplot, the horizontal axis represents the time interval, and the vertical axis represents the normalized magnitude. Correctly classified results are marked in green, while misclassified results are marked in red. The results indicate that the model is capable of correctly identifying different shapes of space objects. The experiments also confirm that shape characteristics influence the properties of light curves, and that light curves have the capability to invert the shape of space objects.

To evaluate the performance of the PIT model, we conducted comparative experiments using classic algorithms such as CNN, LSTM, FCN, Multilayer Perceptron (MLP), Residual Network (ResNet), RF, and LSTM-FCN. All eight models were provided with the same photometric data and the same set of physical features as input. To minimize the influence of other factors, we followed an identical experimental procedure, including data preprocessing, feature selection, and dataset splitting policies, differing only in the model architecture. To ensure a fair and objective comparison, we performed independent grid searches over model-specific hyperparameters—such as learning rate, network depth, and hidden dimension—rather than using a unified configuration, and selected the optimal parameter sets that balance accuracy and efficiency. The learning rate of 0.001 was found to be consistently favorable for all baseline models. In terms of architecture, the CNN was built with 10 layers, the LSTM with a 6-layer bidirectional structure, the FCN with 6 convolutional layers, the MLP with 6 fully connected layers, and the ResNet with a 1D adaptation of ResNet-18; the Random Forest utilized 100 trees with a maximum depth of 15,

while the LSTM-FCN integrated 2 convolutional layers with a 2-layer bidirectional LSTM. Table 2 reports the accuracy of each algorithm.

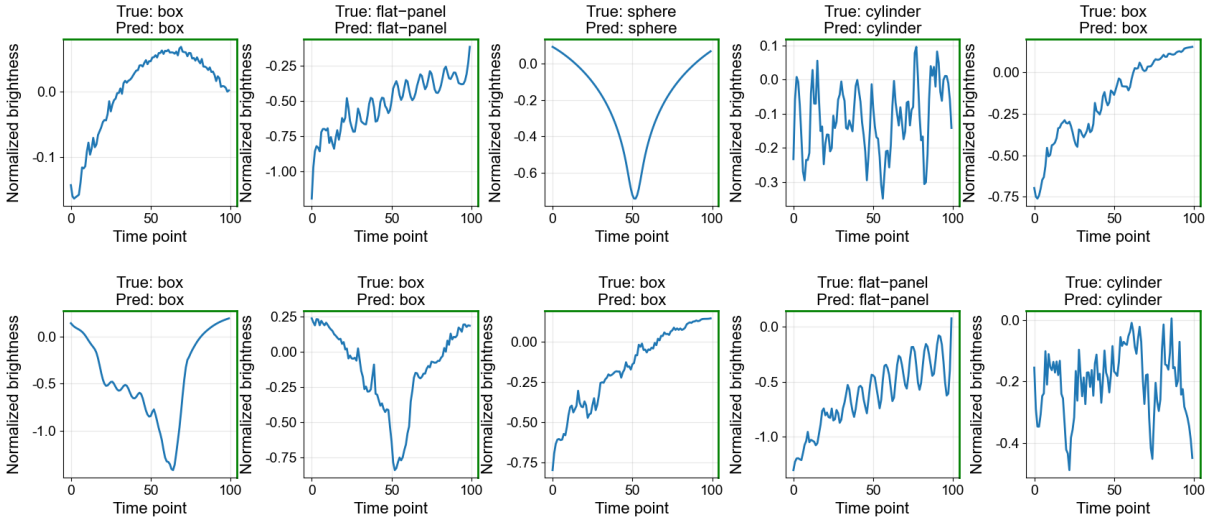



**Figure 7.** Classification results of ten random space objects.

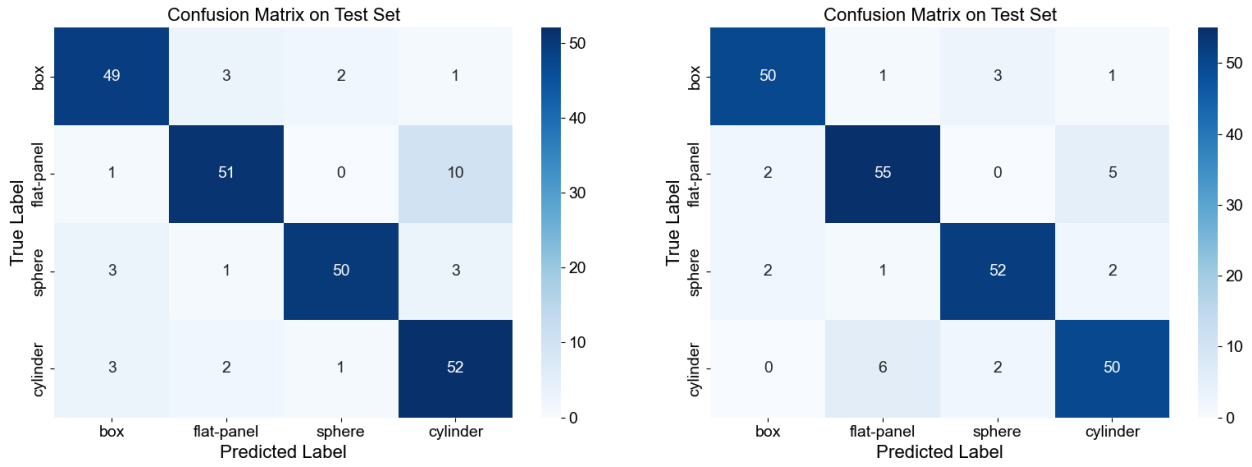
**Table 2.** The accuracy of the algorithms.

| **Algorithm** | CNN | LSTM | FCN | MLP | ResNet | RF | LSTM-FCN | PIT |
|---|---|---|---|---|---|---|---|---|
| **Accuracy** | 84.91% | 82.76% | 83.62% | 83.33% | 87.93% | 87.50% | 87.07% | 89.22% |

The results show that the proposed PIT model achieves an accuracy improvement of 4.31% over CNN, 6.46% over LSTM, 5.60% over FCN, 5.89% over MLP, 1.29% over ResNet, 1.72% over RF, and 2.15% over LSTM-FCN, with an average improvement of 3.61%. Compared with classical algorithms such as CNN and LSTM, the physics-aware self-attention mechanism in PIT exhibits superior capability in capturing long-range light curve patterns, enabling global temporal modeling. By explicitly embedding physical priors into the Transformer architecture, PIT effectively integrates temporal dynamic information with global physical attributes through the physics-aware attention mechanism and gating units, thereby enhancing the discriminative ability for subtle shape differences in light/curves.

To evaluate the performance of the PIT classification model, we employ the confusion matrix, Precision–Recall (PR) curve, Receiver Operating Characteristic (ROC) curve, confidence distribution histogram, and heatmap as performance metrics of the algorithm, and contrast these results with those obtained from the classic LSTM-FCN algorithm.

The confusion matrices are shown in Figure 8. The values in the cells represent the number of instances with true labels classified as each predicted label. The darker the blue color of a cell, the higher the number of correct classifications. As indicated by the confusion matrices, our PIT model achieves better classification performance on four object shapes than the conventional LSTM-FCN. The flat-panel class obtains a 6.45-percentage-point improvement in precision, and its misclassifications to cylinder are halved. The precision of the sphere class increases by 3.51 percentage points, while the box class sees a modest performance gain. Despite a slight drop in the precision of the cylinder class, cross misclassifications between the two categories decline and the overall classification becomes more balanced. Limited residual errors result from short light curve observation time and indistinct features, and the PIT model exhibits greater robustness than LSTM-FCN in this case.




(**a**) (**b**)

**Figure 8.** (**a**) Confusion Matrix of LSTM-FCN. (**b**) Confusion Matrix of PIT.

For the PR curve, the horizontal axis represents recall and the vertical axis represents precision; a high-performance algorithm should achieve both high precision and high recall. For the ROC curve, the horizontal axis represents the false positive rate (FPR) and the vertical axis the true positive rate (TPR); the higher the TPR and the lower the FPR, the better the algorithm performance. Both curves were plotted using the one-vs-rest (OvR) strategy, where each class is treated as positive against the remaining three classes.

As shown in Figure 9, the proposed PIT model outperforms the classic LSTM-FCN model across all object shape classes. For the PIT model, the per-class Average Precision (AP) reaches 0.9771 for box, 0.9222 for flat-panel, 0.9726 for sphere, and 0.9537 for cylinder, yielding a macro-average AP of 0.9564. In comparison, the LSTM-FCN model achieves a macro-average AP of 0.9312, with per-class AP values of 0.9472 (box), 0.9036 (flat-panel), 0.9517 (sphere), and 0.9221 (cylinder). The PIT model improves the macro-average AP by 2.52 percentage points, demonstrating stronger overall precision–recall trade-off performance. Similarly, the area under the ROC curve (AUC) further confirms the superiority of PIT. The PIT model obtains a macro-average AUC of 0.9839, with per-class AUC values of 0.9910 (box), 0.9796 (flat-panel), 0.9852 (sphere), and 0.9798 (cylinder). In contrast, the LSTM-FCN model achieves a macro-average AUC of 0.9716, with per-class AUC values of 0.9688 (box), 0.9713 (flat-panel), 0.9722 (sphere), and 0.9741 (cylinder). The nearly ideal shapes of both PR and ROC curves, combined with the high AP and AUC values close to 1, indicate that the PIT model maintains stable recall while achieving extremely high precision, thus demonstrating excellent discriminative ability for all object classes.

As shown in Figure 10, the confidence distribution histograms and classification report heatmaps demonstrate that the PIT model achieves competitive performance compared with the conventional LSTM-FCN. The PIT model concentrates most correct predictions at confidence values above 0.9, whereas misclassified samples correspond to relatively low confidence levels. Such a distribution enables reasonable control of prediction uncertainty and stable model prediction performance. In terms of quantitative evaluation metrics, the PIT model produces more balanced results across all four object categories. The box class gains higher precision and F1-score, with values rising from 0.875 to 0.926 and from 0.883 to 0.917 respectively. The flat-panel class achieves improved recall and F1-score, which increase from 0.823 to 0.887 and from 0.857 to 0.880. The sphere class maintains steady and balanced classification performance. The cylinder class obtains consistent metric improvements and fewer cross-category misclassifications despite a relatively mild performance increment. These phenomena validate the robustness of the PIT model. The

combination of physical priors and Transformer architecture helps the model capture subtle differences in light curve physical characteristics of diverse space objects, supporting stable and reliable shape classification capability.

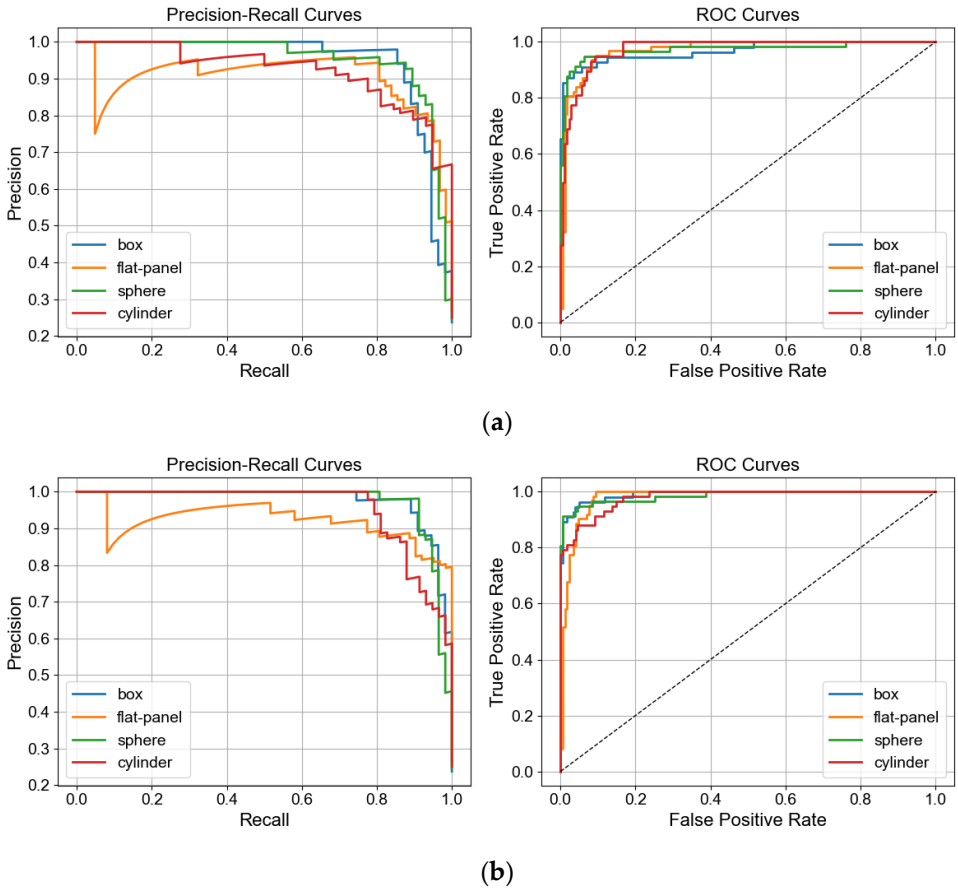



**Figure 9.** (**a**) PR curves and ROC curves of LSTM-FCN; (**b**) PR curves and ROC curves of PIT. The dashed line represents the diagonal reference line. A reliable classifier should have its ROC curve located above this dashed line.

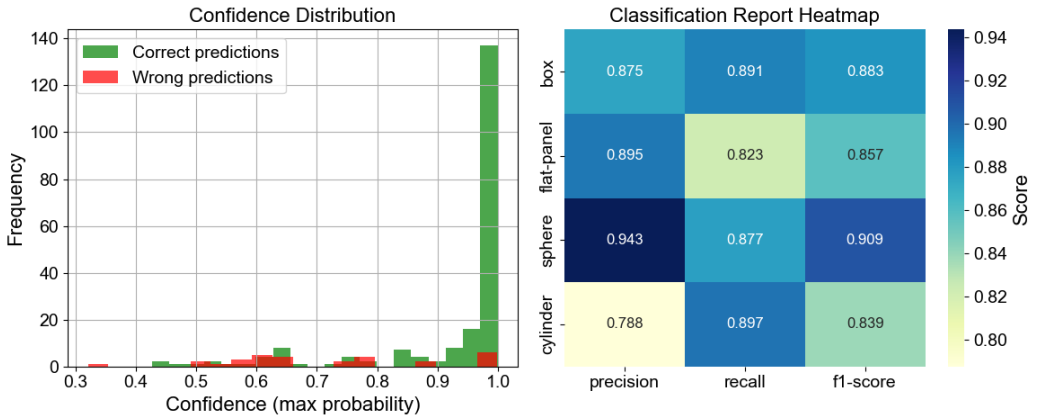
The results of applying the model only to the measured data in the test set are shown in Table 3.

**Table 3.** Results on Measured Data.

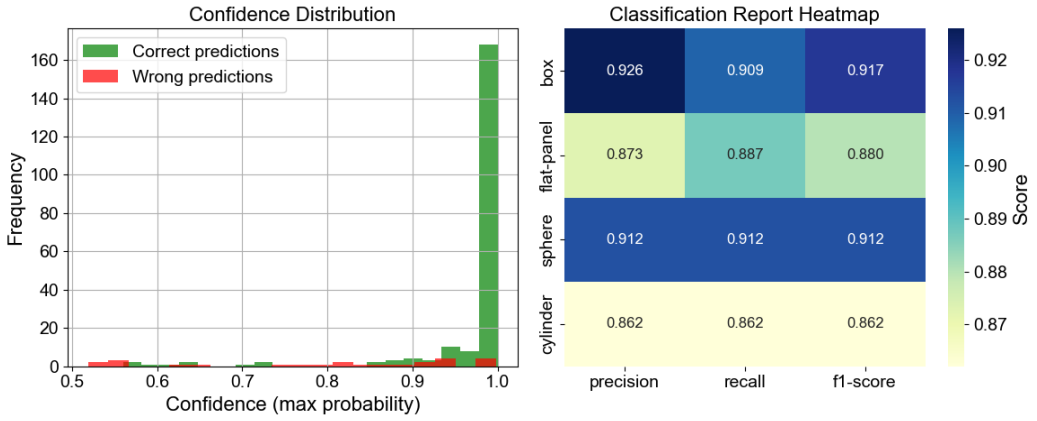
| Objects | Predicted Class | Real Class | Result |
|---|---|---|---|
| 37384_1 | box | box | TRUE |
| 45366_1 | cylinder | flat-panel | FALSE |
| 36605_1 | cylinder | cylinder | TRUE |
| 36605_2 | cylinder | cylinder | TRUE |
| 45366_2 | flat-panel | flat-panel | TRUE |
| 8820_1 | sphere | sphere | TRUE |
| 45088_1 | flat-panel | flat-panel | TRUE |
| 45366_3 | flat-panel | flat-panel | TRUE |
| 45088_2 | cylinder | flat-panel | FALSE |
| 36605_3 | cylinder | cylinder | TRUE |
| 45088_2 | cylinder | flat-panel | FALSE |
| 45088_3 | cylinder | flat-panel | FALSE |
| 45088_4 | flat-panel | flat-panel | TRUE |
| 36605_4 | flat-panel | cylinder | FALSE |

**Table 3.** *Cont.*

| Objects | Predicted Class | Real Class | Result |
|---|---|---|---|
| 36605_5 | cylinder | cylinder | TRUE |
| 45088_5 | flat-panel | flat-panel | TRUE |
| 45366_4 | flat-panel | flat-panel | TRUE |
| 8820_2 | box | sphere | FALSE |
| 36605_6 | cylinder | cylinder | TRUE |
| 45366_5 | flat-panel | flat-panel | TRUE |
| 37384_2 | box | box | TRUE |
| 44443_1 | sphere | sphere | TRUE |
| 44443_2 | flat-panel | sphere | FALSE |




(**a**)




(**b**)

**Figure 10.** (**a**) Confidence Distribution and Classification Report Heatmap of LSTM-FCN; (**b**) Confidence Distribution and Classification Report Heatmap of PIT.

In the table, the first column represents the object ID and index, where different indices denote different light curves of the same object; the second column is the predicted class, the third column is the true class, and the fourth column indicates the result. Among these, the light curves of object 44443 were simulated using real historical TLE data. Through analysis, it was found that for some misclassified objects (e.g., 45366_1), light curves from multiple passes within 48 h were concatenated, each containing few data points with long temporal intervals. This may be caused by different observational geometries and atmospheric conditions, which introduce incorrect temporal dependencies into the data and thus affect the classification results. For some objects (e.g., 8820_1), the measured data contained too few points, making discrimination difficult. The accuracy of the PIT

algorithm on the small-scale measured data is 69.57% (with a 95% confidence interval), while the classical LSTM-FCN algorithm achieves an accuracy of 52.17% on the same measured data, representing an improvement of 14.4% points. Although the limited sample size of the measured data, together with the significant variations in light curves for the same target induced by different observational geometries and atmospheric conditions, implies that this accuracy improvement does not yet meet the threshold for strict statistical significance, this result still provides a preliminary validation of the algorithm's promising potential in real-world sparse and high-noise observational scenarios. With the continued accumulation of measured data samples in the future, the algorithm's performance in real-world applications is expected to be assessed with greater accuracy and reliability.

To investigate the importance of physical information, we conducted an ablation experiment using five independent training runs with different random seeds on the same dataset, comparing the results of the PIT model and the Transformer model without physical gating. The results are summarized in Table 4. The PIT model consistently outperformed the baseline across all seeds, achieving an average accuracy improvement of 1.43%, rising from 86.71% to 88.14%. These results indicate that the incorporation of physical information enhances model performance and robustness across different initializations. Although the accuracy improvement is modest, for a large population of space objects, even a small gain can lead to the correct shape feature of a substantial number of objects.

**Table 4.** Ablation experiment results.

| Model | Accuracy with Seed 1 | Accuracy with Seed 2 | Accuracy with Seed 3 | Accuracy with Seed 4 | Accuracy with Seed 5 |
|---|---|---|---|---|---|
| Transformer model without physical gating | 88.79% | 87.61% | 85.41% | 84.98% | 86.75% |
| PIT | 89.22% | 88.46% | 86.27% | 88.41% | 90.17% |

The PCA cumulative variance curves for the four shape classes are shown in Figure 11. It can be observed that the features exhibit clear class-discriminative properties and favorable low-dimensional separability. All four categories display a consistent, rapid convergence trend in their cumulative variance curves. Specifically, the box class reaches the 85% cumulative variance threshold at four principal components, while the cylinder, sphere, and flat-panel classes reach this threshold between four and five principal components. By seven principal components, all classes achieve over 95% explained variance, and by eight to nine components, the cumulative variance exceeds 98% for all shape classes. This indicates that the extracted features possess good clustering properties in low-dimensional space and can effectively characterize light curve variations of different object shapes with low redundancy.

The weighted contribution heatmap is shown in Figure 12. This weighted contribution metric is a custom feature importance measure derived from principal component analysis rather than SHAP values, learnable network weights or attention maps. For each object category, the extracted physical features are standardized first, followed by PCA decomposition to obtain component loadings and corresponding variance explanation ratios. The weighted contribution of each physical feature is calculated as the sum of the squared loading coefficients multiplied by the variance explanation ratio of the first several principal components, where squared loadings reflect the absolute influence of original features on principal components and variance ratios assign greater importance to components carrying more effective information. This post-hoc statistical approach quantifies the capability of each physical feature to explain intra-class data variance and characterize class-discriminative properties. The analysis of weighted contributions of physical features

reveals that key discriminative features vary across different shape categories. For box objects, peak ratio, symmetry, and information entropy contribute the most. For flat-panel objects, standard deviation and regularity serve as the dominant features, with kurtosis playing a secondary role. For spherical objects, standard deviation, symmetry, and regularity are the most prominent contributors, while information entropy shows the lowest contribution. For cylindrical objects, symmetry, kurtosis, and mean value present relatively high contributions, whereas information entropy shows the weakest influence. This differentiated distribution of feature contributions confirms the effectiveness of the physical gating mechanism in the PIT model. The model can adaptively assign weights to physical features for different shapes, prioritizing the learning of attributes most discriminative for each category, thereby supporting accurate shape recognition of space objects.

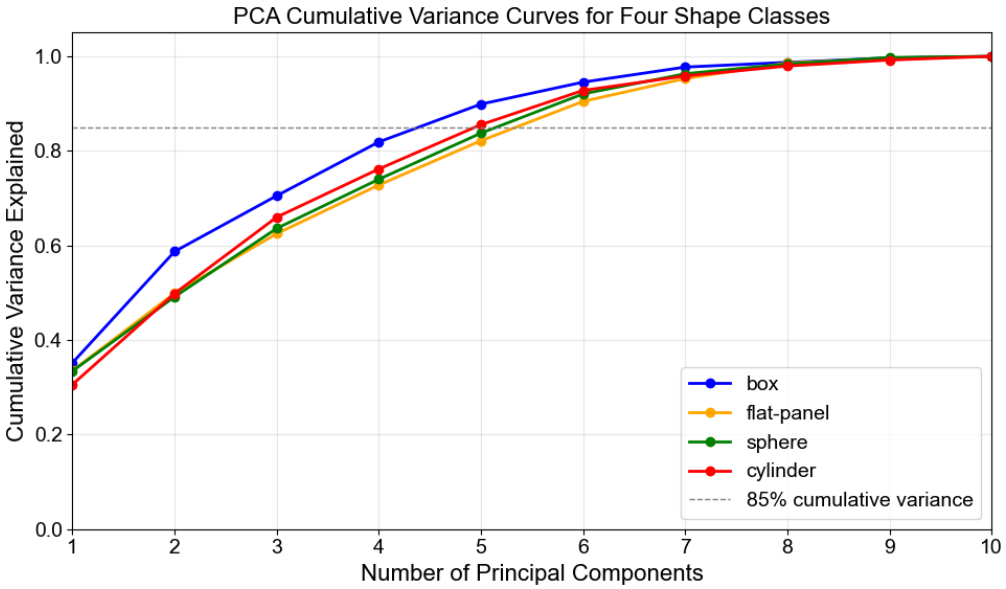



**Figure 11.** PCA cumulative variance curves.

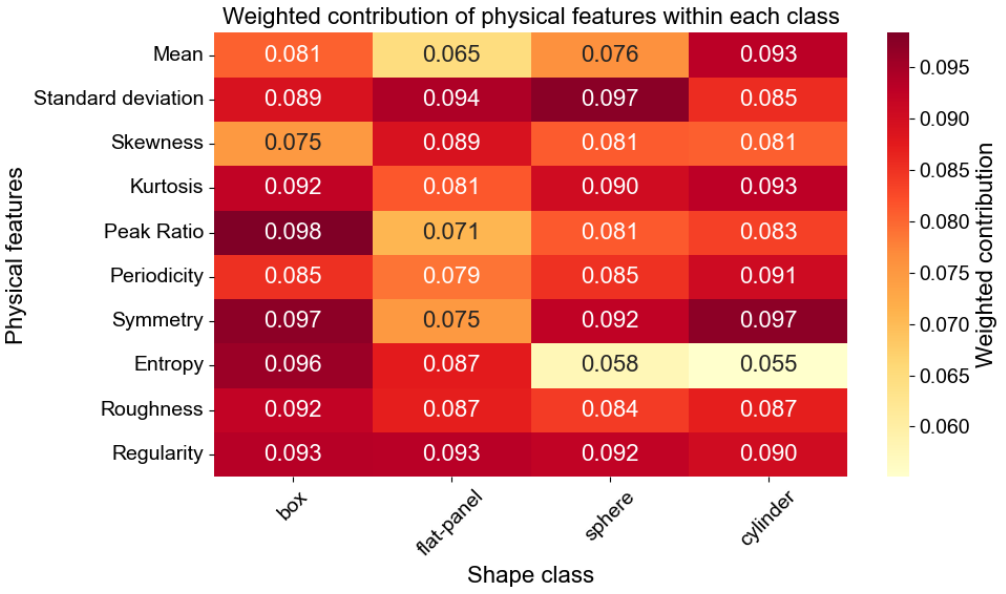



**Figure 12.** Weighted contribution heatmap.

In summary, the PIT model exhibits strong performance, offering advantages such as high accuracy and high reliability. It addresses the issues of weak generalization and poor

interpretability inherent in traditional data-driven models, which tend to neglect physical priors. Consequently, the model achieves precise recognition of object shapes.

## 5. Conclusions

We propose a Physics-Informed Transformer (PIT) model for space object configuration classification. The model takes light curves as input and employs a dual-branch encoding architecture to encode sequential and physical information separately. A multi-head physics-aware self-attention mechanism (MHPA) is introduced to dynamically modulate the self-attention output using physical information as gating signals, thereby organically integrating data-driven learning and physical information within a unified deep learning framework. The PIT model does not rely on additional information such as orbital parameters; it achieves end-to-end recognition of four typical space object shapes, namely box, flat-panel, sphere, and cylinder, using only photometric data and associated physical information. It addresses the issues of weak generalization and poor interpretability inherent in traditional data-driven models, which tend to neglect physical priors, and possesses superior capability in capturing long-range dependencies compared to traditional LSTM and CNN algorithms. The model offers the advantages of high accuracy and reliability.

We conducted experiments using a hybrid dataset consisting of 2224 light curves after data augmentation, which includes simulation data from Space Engineering University and measured data from multiple observation stations. After preprocessing steps including resampling, filtering, normalization, and data augmentation, the PIT model was trained and validated. The results demonstrate that the proposed PIT model achieves a test accuracy of 89.22%, outperforming classical algorithms with improvements of 4.31% over CNN, 6.46% over LSTM, 5.60% over FCN, 5.89% over MLP, 1.29% over ResNet, 1.72% over RF, and 2.15% over LSTM-FCN, representing an average improvement of 3.61%. Compared with the LSTM-FCN baseline, the PIT model attains a higher macro-average AP of 0.9564 versus 0.9312 and a higher macro-average AUC of 0.9839 versus 0.9716. The confusion matrix shows a highly diagonal distribution with reduced cross-category misclassifications. The confidence distribution histogram indicates that most correctly predicted samples have confidence above 0.9, while misclassified samples exhibit lower confidence. The classification report heatmap reveals balanced precision, recall, and F1-scores across the four object classes. Ablation experiments over five independent runs show that incorporating the physical gating mechanism improves the average accuracy by 1.43%, rising from 86.71% to 88.14%, resulting in a slight performance gain. Although performance on the limited measured test set is lower than on simulated data, it still represents a 14.4% point improvement over LSTM-FCN, demonstrating enhanced generalization in realistic, noisy conditions. PCA analysis indicates that the extracted physical features exhibit good low-dimensional separability, and the weighted contribution heatmap reveals that different shape classes rely on distinct feature subsets, validating the adaptive gating mechanism. These results collectively confirm that the PIT model achieves high accuracy and strong robustness in space object shape recognition, effectively addressing the weak generalization and poor interpretability of traditional data-driven models that neglect physical priors.

However, this study mainly focuses on space objects with typical shapes such as box, flat-panel, sphere, and cylinder. In the future, we will consider incorporating higher-order physical priors, including spectral features and orbital motion, to extend the model's recognition capability to complex configurations.

**Author Contributions:** Conceptualization, M.L., L.Z., R.L., Y.L. and H.G.; methodology, M.L., H.Z. (Huaili Zhang), H.Z. (Haijing Zheng) and S.D.; software, M.L., Y.Z., Z.D. and R.Z.; validation, M.L., L.Z., R.L., Y.L., H.G. and H.Z. (Haijing Zheng); formal analysis, M.L. and L.Z.; investigation, M.L., Y.Z., Z.D. and R.Z.; resources, M.L., L.Z., Y.L., H.G., S.D. and Y.Z.; data curation, M.L., S.D. and Y.Z.;

writing—original draft preparation, M.L.; writing—review and editing, M.L., L.Z., R.L., Y.L., H.G. and H.Z. (Huaili Zhang); visualization, M.L. and S.D.; supervision, M.L. and L.Z.; project administration, M.L., L.Z., R.L. and Y.L.; funding acquisition, M.L., H.Z. (Huaili Zhang) and S.D. All authors have read and agreed to the published version of the manuscript.

**Funding:** This research was funded by the National Key Laboratory of Space Security, grant number ZN04-02-2502; the National Natural Science Foundation of China, grant number 12503114, 12203078; the Key Laboratory of Intelligent Space TTC&O (Space Engineering University), Ministry of Education, grant number CYK2025-01-09; the Jilin Province Science and Technology Development Plan Item, grant number 20250205078GH; the Chinese Academy of Sciences President's International Fellowship Initiative, grant number 2026PVA00044; and the Chinese Academy of Sciences National Astronomical Observatories Changchun Observatory 2025 Youth Exploration Fund.

**Data Availability Statement:** The original data can be shared upon reasonable request to the corresponding author.

**Acknowledgments:** We would like to thank the Changchun Institute of Optics, Fine Mechanics and Physics, Chinese Academy of Sciences, and the Changchun Observatory, National Astronomical Observatories, Chinese Academy of Sciences, for providing some of the measured data of space objects.

**Conflicts of Interest:** The authors declare no conflicts of interest.

## References

1. Wang, Z.; Han, Y.; Zhang, Y.; Hao, J.; Zhang, Y. Classification and Recognition Method of Non-Cooperative Objects Based on Deep Learning. *Sensors* **2024**, *24*, 583. [CrossRef] [PubMed]
2. Kennewell, J.A.; Vo, B.N. An overview of space situational awareness. In Proceedings of the 16th International Conference on Information Fusion, Istanbul, Turkey, 9–12 July 2013.
3. Bradley, B.K.; Axelrad, P. Lightcurve inversion for shape estimation of geo objects from space-based sensors. In Proceedings of the 24th International Symposium on Space Flight Dynamics, Laurel, MD, USA, 5–9 May 2014.
4. Li, R.; Li, H.; Shu, P.; Li, Y. Research Progress on Estimating Space Objects Characteristics Using Ground-based Observation Data. *Chin. J. Space Sci.* **2025**, *45*, 1629–1643. [CrossRef]
5. Mallama, A. A Flat-Panel Brightness Model for the Starlink Satellites and Measurement of their Absolute Visual Magnitude. *arXiv* **2020**, arXiv:2003.07805.
6. Otsubo, T.; Matsuo, K. Precise orbit determination of non-standard SLR satellites: (1) Satellite shape models. In Proceedings of the Japan Geoscience Union Meeting 2022, Chiba, Japan, 22 May–3 June 2022.
7. Lu, Y.; Zhao, C. The Basic Shape Classification of Space Debris with Light Curves. *Chin. Astron. Astrophys.* **2021**, *45*, 190–208. [CrossRef]
8. Wetterer, C.J.; Jah, M. Attitude Estimation from Light Curves. *J. Guid. Control Dyn.* **2009**, *32*, 1648.
9. Liu, H.; Du, X. Development of shape estimation of spacetarget based on lightcurve inversion. *Chin. Opt.* **2015**, *8*, 744–754.
10. Adriano, A.; Scott, K.A.; Oqab, H.; Dietrich, G.; Azad, N.L. Neural Networks for Space Debris Classification. *Expert Syst.* **2026**, *43*, e70180.
11. Linares, R.; Crassidis, J.L.; Jah, M.K.; Kim, H. Astrometric and Photometric Data Fusion for Resident Space Object Orbit, Attitude, and Shape Determination Via Multiple-Model Adaptive Estimation. In Proceedings of the AIAA Guidance, Navigation, and Control Conference, Toronto, ON, Canada, 2–5 August 2010.
12. Linares, R.; Jah, M.K.; Crassidis, J.L. Inactive space object shape estimation via astrometric and photometric data fusion. *Adv. Astronaut. Sci.* **2012**, *143*, 217–232.
13. Linares, R. Probabilistic Identification and Discrimination of Deep Space Objects via Astrometric and Photometric Data Fusion. Ph.D. Thesis, State University of New York at Buffalo, Buffalo, NY, USA, 2013.
14. Linares, R.; Jah, M.K.; Crassidis, J.L.; Leve, F.A.; Kelecy, T. Astrometric and photometric data fusion for inactive space object mass and area estimation. *Acta Astronaut.* **2014**, *99*, 1–15. [CrossRef]
15. Wetterer, C.J.; Hunt, B.; Kervin, P.; Jah, M. Comparison of Unscented Kalman Filter and Unscented Schmidt Kalman Filter in predicting attitude and associated uncertainty of a geosynchronous satellite. In Proceedings of the Advanced Maui Optical and Space Surveillance Technologies Conference, Maui, HI, USA, 9–12 September 2014.
16. Wang, Y.; Du, X.; Fan, C. Progress of light curve inversion technology for resident space object characteristics. *Chin. Sci. Bull.* **2017**, *62*, 1578. [CrossRef]

17. Liu, H. Research on the Spatial Object Shape Inversion Method Based on Light Curves. Master's Thesis, Equipment Academy, Beijing, China, 2016.
18. Liu, H.; Li, Y.; Sun, G.; Huang, C. Research on Multiple Model Adaptive Estimation Space Object Shape Inversion. *J. Northwest. Polytech. Univ.* **2018**, *36*, 75–79.
19. Anderson, J.T.; Gaylor, D.E.; Th, D.I.; Russell, R.P.; Schadegg, M. Resident Space Object Feature Identification using Hierarchical Mixtures of Experts. In Proceedings of the Advanced Maui Optical and Space Surveillance Technologies (AMOS) Conference, Maui, HI, USA, 10–13 September 2013.
20. Gaylor, D.; Anderson, J. Use of Hierarchical Mixtures of Experts to Detect Resident Space Object Attitude. In Proceedings of the Advanced Maui Optical and Space Surveillance Technologies (AMOS) Conference, Maui, HI, USA, 9–12 September 2014.
21. Fan, S.; Friedman, A.M.; Frueh, C. Satellite Shape Recovery from Light Curves with Noise. In Proceedings of the Advanced Maui Optical and Space Surveillance Technologies (AMOS) Conference, Maui, HI, USA, 17–20 September 2019.
22. Cabrera, D.V.; Utzmann, J.; Förstner, R. Inversion of the shape of space debris from non-resolved optical measurements within SPOOK. In Proceedings of the Advanced Maui Optical and Space Surveillance Technologies (AMOS) Conference, Maui, HI, USA, 14–17 September 2021.
23. Chaudhary, A.B.; Payne, T.E.; Lucas, K.; Mutschler, S.; Vincent, T.; Dao, P.; Murraykrezan, J. Point Pairing Method Based on the Principle of Material Frame Indifference for the Characterization of Unknown Space Objects using Non-Resolved Photometry Data. In Proceedings of the Advanced Maui Optical and Space Surveillance Technologies (AMOS) Conference, Maui, HI, USA, 10–13 September 2013.
24. Chaudhary, A.B.; Payne, T.E.; Lucas, K.; Kinateder, K.K.; Dao, P.; Murraykrezan, J. Propagation of Bayesian Belief for Near-Real Time Statistical Assessment of Geosynchronous Satellite Status Based on Non-Resolved Photometry Data. In Proceedings of the Advanced Maui Optical and Space Surveillance Technologies (AMOS) Conference, Maui, HI, USA, 9–12 September 2014.
25. Mcmahon, J.W.; Scheeres, D.J. Shape Estimation from Lightcurves including Constraints from Orbit Determination. In Proceedings of the Advanced Maui Optical and Space Surveillance Technologies (AMOS) Conference, Maui, HI, USA, 20–23 September 2016.
26. Robinson, L. Light Curve Inversion: Determining the Shape of Human-Made Space Objects. *J. Purdue Undergrad. Res.* **2022**, *12*, 17. [CrossRef]
27. Tang, Y.; Ying, C.; Xia, C.; Zhang, X.; Jiang, X. Asteroid shape inversion with light curves using deep learning. *Astron. Astrophys.* **2025**, *696*, A55. [CrossRef]
28. Charles, W.; Clayton, S.; James, S. Lightcurve inversion program for non-resolved space object identification. In Proceedings of the Advanced Maui Optical and Space Surveillance Technologies (AMOS) Conference, Maui, HI, USA, 10–14 September 2006.
29. Payne, T.; Gregory, S.; Luu, K. SSA Analysis of GEOS Photometric Signature Classifications and Solar Panel Offsets. In Proceedings of the Advanced Maui Optical and Space Surveillance Technologies (AMOS) Conference, Maui, HI, USA, 10–14 September 2006.
30. Zhao, X.; Zheng, J.; Mao, Y.; Yu, Y.; Wang, K.; Wen, C. GEOS Photometric Signature Classifications Based on Observations of FocusGEO Telescopes. *Chin. J. Space Sci.* **2022**, *42*, 136–143. [CrossRef]
31. Singh, N.; Horwood, J.; Aristoff, J.; Murray-Krezan, J. Athena: A data-driven anomaly detection and space object classification tool for SSA. In Proceedings of the 26th AAS/AIAA Space Flight Mechanics Meeting, Napa, CA, USA, 14–18 February 2016.
32. Howard, M.; Klem, B.; Gorman, J. RSO Characterization with Photometric Data Using Machine Learning. In Proceedings of the Advanced Maui Optical and Space Surveillance Technologies (AMOS) Conference, Maui, HI, USA, 9–12 September 2014.
33. Lu, Y.; Zhao, C. The Basic Shape Classification of Space Debris with Light Curves. *Acta Astron. Sin.* **2020**, *61*, 64.
34. Jia, B.; Pham, K.D.; Blasch, E.; Shen, D.; Wang, Z.; Chen, G. Space Object Classification Using Fused Features of Time Series Data. In Proceedings of the Advanced Maui Optical and Space Surveillance Technologies (AMOS) Conference, Maui, HI, USA, 19–22 September 2017.
35. Linares, R.; Furfaro, R.; Reddy, V. Space Objects Classification via Light-Curve Measurements Using Deep Convolutional Neural Networks. *J. Astronaut. Sci.* **2020**, *67*, 1063–1091. [CrossRef]
36. Huo, Y.; Li, Z.; Fang, Y. Space object shape characterization from photometric data using recurrent neural network. In Proceedings of the 4th International-Academy-of-Astronautics Conference on Dynamics and Control of Space Systems (DyCoSS '2018), Changsha, China, 21–23 May 2018.
37. Furfaro, R.; Linares, R.; Reddy, V. Space Objects Classification via Light-Curve Measurements: Deep Convolutional Neural Networks and Model-based Transfer Learning. In Proceedings of the Advanced Maui Optical and Space Surveillance Technologies (AMOS) Conference, Maui, HI, USA, 11–14 September 2018.
38. Mcquaid, I.; Merkle, L.; Borghetti, B.; Cobb, R.; Fletcher, J. Space Object Identification using Deep Neural Networks. In Proceedings of the Advanced Maui Optical and Space Surveillance Technologies (AMOS) Conference, Maui, HI, USA, 11–14 September 2018.
39. Ismail Fawaz, H.; Forestier, G.; Weber, J.; Idoumghar, L.; Muller, P.A. Deep learning for time series classification: A review. *Data Min. Knowl. Disc.* **2019**, *33*, 917–963. [CrossRef]
40. Allworth, J.; Windrim, L.; Bennett, J.; Bryson, M. A transfer learning approach to space debris classification using observational light curve data. *Acta Astronaut.* **2021**, *181*, 301–315. [CrossRef]

41. Kerr, E.; Petersen, E.G.; Talon, P.; Petit, D.; Dorn, C.; Eves, S. Using AI to Analyse Light Curves for GEO Object Characterisation. In Proceedings of the Advanced Maui Optical and Space Surveillance Technologies (AMOS) Conference, Maui, HI, USA, 14–17 September 2021.
42. Badura, G.P.; Valenta, C.R.; Gunter, B. Convolutional Neural Networks for Inference of Space Object Attitude Status. *J. Astronaut. Sci.* **2022**, *69*, 593–626. [CrossRef]
43. Qashoa, R.; Lee, R. Classification of Low Earth Orbit (LEO) Resident Space Objects' (RSO) Light Curves Using a Support Vector Machine (SVM) and Long Short-Term Memory (LSTM). *Sensors* **2023**, *23*, 6539. [CrossRef] [PubMed]
44. Zhang, Y.; Wang, J.; Chen, J.; Shi, D.; Chen, X. A Space Non-Cooperative Target Recognition Method for Multi-Satellite Cooperative Observation Systems. *Remote Sens.* **2024**, *16*, 3368. [CrossRef]
45. Majhi, S.; Naik, K.R.; Namrata, K.; Meena, V.; Gowda, D. Machine Learning-Based Classification of Space Debris and Satellites Using Orbital Parameters. In Proceedings of the 2025 IEEE Space, Aerospace and Defence Conference (SPACE), Bangalore, India, 21–23 July 2025.
46. Wang, J.; Jiang, X.; Li, T.; Zhang, X.; Ge, L. Research on optical scattering of radar calibration satellite. *Infrared Laser Eng.* **2020**, *49*, 010500.

**Disclaimer/Publisher's Note:** The statements, opinions and data contained in all publications are solely those of the individual author(s) and contributor(s) and not of MDPI and/or the editor(s). MDPI and/or the editor(s) disclaim responsibility for any injury to people or property resulting from any ideas, methods, instructions or products referred to in the content.